SCIENTIFIC REPORTS

OPEN

Aerosol assisted chemical vapour deposition of gas sensitive SnO$_2$ and Au-functionalised SnO$_2$ nanorods via a non-catalysed vapour solid (VS) mechanism

Stella Vallejos[1], Soultana Selina[2], Fatima Ezahra Annanouch[3,4], Isabel Gràcia[5], Eduard Llobet[3] & Chris Blackman[2]

Tin oxide nanorods (NRs) are vapour synthesised at relatively lower temperatures than previously reported and without the need for substrate pre-treatment, *via* a vapour-solid mechanism enabled using an aerosol-assisted chemical vapour deposition method. Results demonstrate that the growth of SnO$_2$ NRs is promoted by a compression of the nucleation rate parallel to the substrate and a decrease of the energy barrier for growth perpendicular to the substrate, which are controlled via the deposition conditions. This method provides both single-step formation of the SnO$_2$ NRs and their integration with silicon micromachined platforms, but also allows for *in-situ* functionalization of the NRs with gold nanoparticles *via* co-deposition with a gold precursor. The functional properties are demonstrated for gas sensing, with microsensors using functionalised NRs demonstrating enhanced sensing properties towards H$_2$ compared to those based on non-functionalised NRs.

Due to their size dependant properties the synthesis of nanostructures (nanowires (NWs), nanorods (NRs), nanotubes (NTs) and nanobelts (NBs)) has become one of the most active research areas within the nanoscience community. Nanostructured materials, in particular semiconducting metal oxides (SMOx), have demonstrated exceptional optical and electrical properties due to electron and phonon confinement, with higher surface-to-volume ratios, modified surface work function, higher surface reaction activity, better catalytic efficiency and stronger adsorption ability compared to their bulk counterparts[1].

Tin oxide (SnO$_2$) is an intrinsic n-type wide-bandgap SMOx with applications in transparent conducting electrodes, solar cells and gas sensors[2–4]. In particular SnO$_2$ is used in most current commercial resistive gas sensors and is the most studied material in the gas sensing literature, with demonstrated sensitivity to carbon monoxide, hydrogen, ethanol, and nitrogen dioxide, amongst others[3–6].

Nanostructures of SnO$_2$ have been synthetized using various methods, including chemical vapour deposition (CVD)[7–15], thermal evaporation[16–19], laser ablation[20], template (AAO – anodic alumina oxide) assisted electrodepositon[21,22], and liquid-phase methods[23,24]. Among these, vapour-phase synthesis (e.g. CVD) offers potential advantages, including the ability to operate in continuous mode and greater material purity. However CVD routes to nanostructured SnO$_2$ typically require significant amounts of energy to reach the high temperatures required to break strong chemical bonds during the precursor-to-material conversion, which can lead to incompatibilities when integrating this process with microsystems and/or temperature sensitive substrates. To avoid these stringent conditions and allow nanostructure growth at temperatures as low as 650–800 °C[15] or 550–750 °C[8], catalyst seeds on the substrate are used to promote a vapour-liquid-solid (VLS) growth mechanism. However, the need for

[1]SIX Research Centre, Brno University of Technology, Technická 10, Brno, CZ-61600, Czech Republic. [2]Department of Chemistry, University College London, 20 Gordon Street, London, WC1H 0AJ, UK. [3]MINOS-EMaS, Departament d'Enginyeria Electrònica, Universitat Rovira i Virgili, Paisos Catalans 26, Tarragona, 43007, Spain. [4]Aix Marseille Université, CNRS, Université de Toulon, IM2NP UMR 7334, Marseille, France. [5]Instituto de Microelectrónica de Barcelona (IMB-CNM, CSIC), Campus UAB, Barcelona, 08193, Spain. Correspondence and requests for materials should be addressed to S.V. (email: vargas@feec.vutbr.cz) or C.B. (email: c.blackman@ucl.ac.uk)
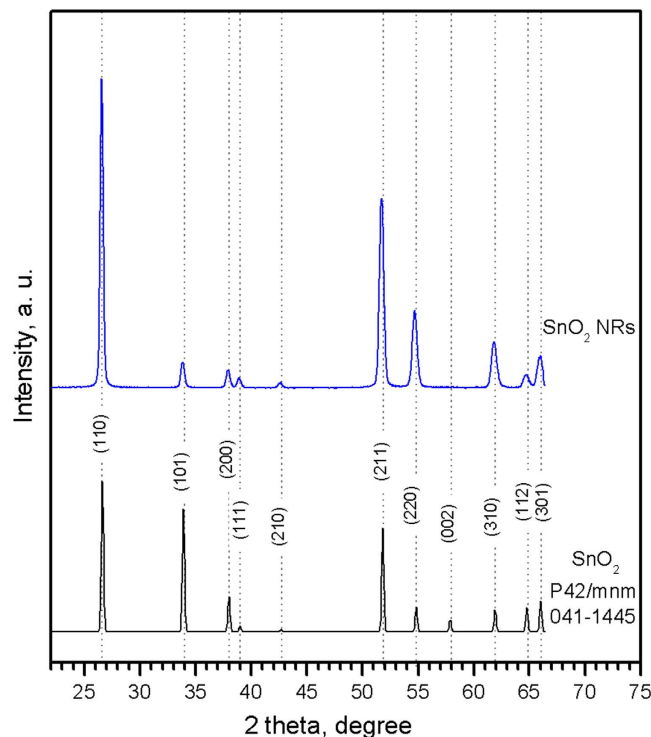
Figure 1. Typical XRD pattern of the SnO$_2$ NRs deposited at temperatures between 300 and 620 °C from a solution of SnCl$_4$·5H$_2$O dissolved in acetone. The diffraction peaks in the data can be indexed to a tetragonal phase (P42/mnm, ICCD card no. 041-1445) of tin oxide.

extra surface pre-treatment processing steps adds potential technological limitations in device fabrication. The formation of nanostructures *via* a vapour-solid (VS) mechanism, in contrast, avoids the use of catalyst seeds and facilitates device fabrication, but the synthesis of tin oxide nanostructures *via* a VS mechanism has so far required the use of very high temperatures in the range of 850 °C and 1150 °C[10,11,13,14,25], or the use of plasma systems to reduce the deposition temperature, both of which can damage fragile substrates[26]. Recently, however, we have recognised that aerosol assisted (AA)CVD (a variant of traditional CVD which uses aerosol droplets to transport the precursor solution to the heated reaction zone) can lead to the formation of tungsten oxide nanostructures *via* a VS mechanism at relatively low onset temperatures, attributed to formation of reactive intermediates during deposition[27]. This method, which works at atmospheric pressure and relies on a solution-based delivery approach, is advantageous over traditional CVD as it allows for a wider range of precursors to be utilised[28]. It also allows for the functionalization of SMOx nanostructures with metal nanoparticles (NPs) in a single processing step *via* co-deposition, which we have demonstrated previously for incorporation of gold[29], platinum[30] or other SMOx (e.g. Cu$_2$O[31] and Fe$_2$O$_3$[32]) nanoparticles segregated at the surface of tungsten oxide nanostructures.

There are very few reports on synthesis of tin oxide or tin oxide composites *via* AACVD, with most referring to the formation of thin films[33–40] rather than nanostructures. The precursors used for the AACVD of tin oxide include common precursors used in traditional CVD[41], such as monobutyltin trichloride (C$_4$H$_9$SnCl$_3$)[38,40], and tin(II) chloride dihydrate (SnCl$_2$·2H$_2$O)[33,42], tin complexes [Sn(18-Cr-6)Cl$_4$][34] and [Sn(H$_2$O)$_2$Cl$_4$](18-Cr-6)[34], or for the deposition of composite films bimetallic complexes such as C$_{29}$H$_{40}$FeO$_2$Sn[37], C$_{35}$H$_{28}$FeO$_2$Sn[37], or [ZnSn(dmae)(dmaeH)$_2$(NO$_3$)Cl$_4$]·2H$_2$O[39].

Here we demonstrate the AACVD of SnO$_2$ nanostructures, in the form of NRs, from a simple commercial tin precursor (SnCl$_4$·5H$_2$O) at atmospheric pressure and exceptionally reduced process temperatures compared to existing VS-based CVD methods. In addition, to enhance the functionality of tin oxide we use the co-deposition opportunities afforded by AACVD to incorporate, in the same single-step, Au NPs at the surface of tin oxide NRs. These non-functionalised (SnO$_2$) and functionalised (Au@SnO$_2$) nanostructures are directly integrated into silicon micromachined platforms (fabricated using Micro-Electro-Mechanical-System (MEMS) technology) and validated for gas sensing, with sensors based on Au-functionalised SnO$_2$ NRs demonstrating enhanced properties.

Results

AACVD of SnO$_2$.   AACVD of SnCl$_4$·5H$_2$O dissolved in acetone or methanol at temperatures between 300 and 675 °C resulted in the formation of adherent uniform greyish films on silicon wafers. XRD analysis confirmed the presence of tetragonal SnO$_2$ (P42/mnm, $a = 4.7380$ Å, $c = 3.1870$ Å, literature P42/mnm space group, $a = 4.7382$ Å, $c = 3.1871$ Å; ICCD card no. 41-1445) for all the films (Fig. 1), except for those deposited from a methanol-based solution at temperatures exceeding 500 °C (Fig. S1), which showed extra diffraction peaks corresponding to metallic tin (I41/amd, $a = 5.8310$ Å, $c = 3.1820$ Å, ICCD card no. 4-673).
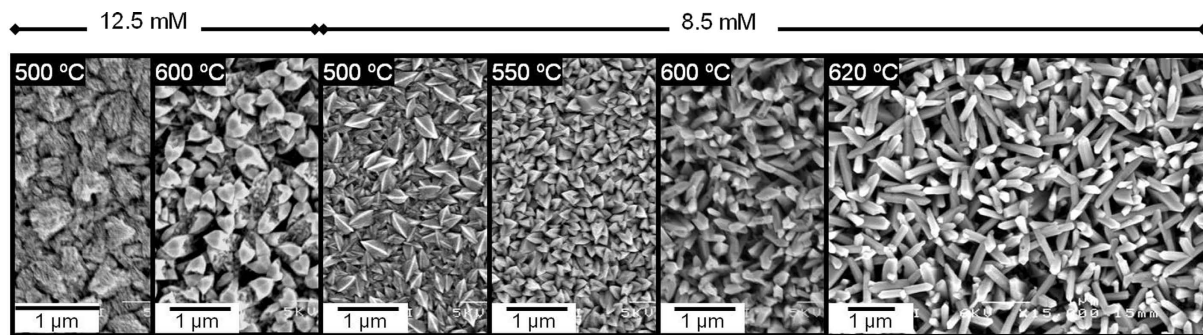
Figure 2. Film morphology observed by SEM images at different solution concentrations and various deposition temperatures.
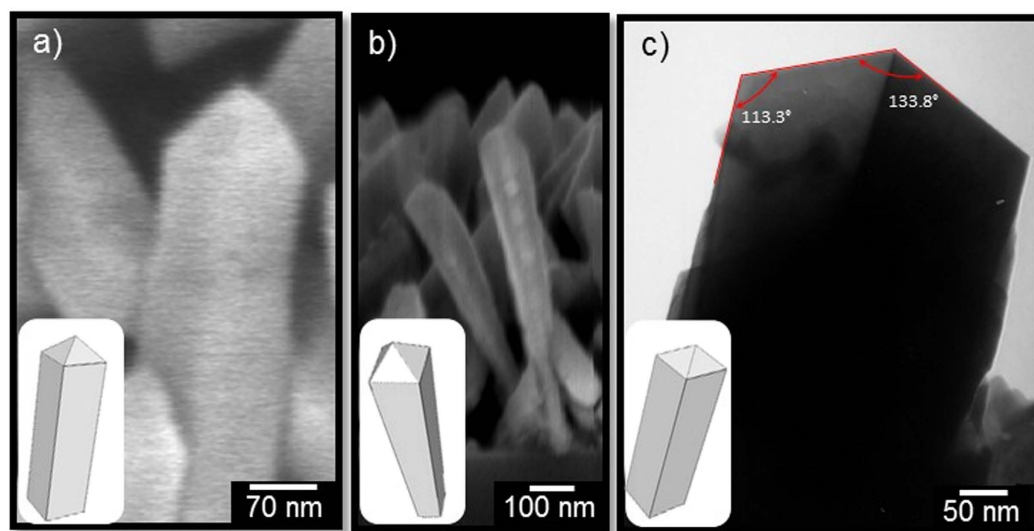

Figure 3. Cross-section SEM (**a,b**) and TEM (**c**) images of SnO$_2$ NRs grown at 620 °C from SnCl$_4$·5H$_2$O dissolved in acetone (8.5 mM). The insets show the NR view models (not to scale).

The morphology of the films was strongly dependent on the deposition temperature, solution concentration and solvent. For instance (Fig. 2), the films deposited from acetone-based solution (12.5 mM) displayed uneven morphology at 500 °C and porous structures with twinned crystallites at 600 °C, whereas the films deposited from lower solution concentration (8.5 mM) showed the formation of porous films with defined crystallites at 500 °C, a high density of leaf-like structures at 550 °C, and the formation of a high density of NRs at 600 °C. An increase in temperature from 600 °C to 620 °C improved the definition of the NRs, and above this temperature (up to 675 °C) the structures suffered deformations with less material deposited on the substrate, most likely due to homogeneous gas-phase reaction resulting in the formation of powder and the action of thermophoretic forces. A further decrease of solution concentration to 4.3 mM ended-up without visible film deposition. Similar test were carried out for methanol-based solutions, which produced porous films for solution concentrations of 12.5 and 8.5 mM in the temperature range of 300 °C and 675 °C (Fig. S2), and no visible deposition when the concentration was decreased to 4.3 mM.

Estimation of the energy activation for the perpendicular growth (E_a^d) of the films[43] *via* the Arrhenius equation indicated lower E_a^d for films grown from acetone-based solutions (16.2 kJ/mol) compared to films grown from the methanol-based solutions (27.4 kJ/mol), the latter being in agreement with the value reported in the literature (24.12 kJ/mol)[44] for the CVD of planar SnO$_2$ films from SnCl$_4$·5H$_2$O.

SnO$_2$ NRs. Detailed examination of the NRs formed at 620 °C *via* AACVD suggest that the structures have a prism-like morphology terminated in a pyramidal cap (Fig. 3a), with a total length of ~700 nm and apparently wider sides at the highest part of the prism (~100 nm) in contrast to the base (Fig. 3b), corresponding to an aspect ratio of approximately 7. TEM imaging of the NRs end-cap indicates a similar morphology to that observed by SEM with an apex and lateral angle of 133.8° and 113.3°, respectively (Fig. 3c). These geometrical features are consistent with the models reported previously on the study of octahedral SnO$_2$ structures synthesized from
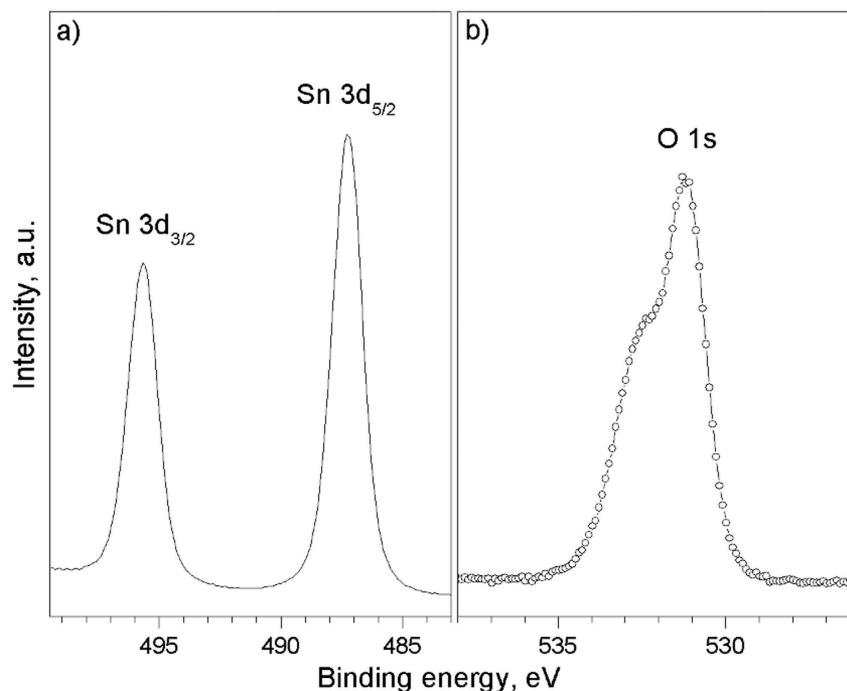
Figure 4. XPS spectrum of the SnO$_2$ NRs grown at 620 °C from SnCl$_4$·5H$_2$O dissolved in acetone (8.5 mM).

SnCl$_4$·5H$_2$O *via* a hydrothermal process[45], and suggest that the pyramidal caps and the prism-like base might be enclosed by the {111} and {110} facets, respectively.

The Sn 3d region of the XPS spectra for the SnO$_2$ NRs (Fig. 4a) exhibited Sn 3d$_{5/2}$ and Sn 3d$_{3/2}$ doublets for binding energies of ~486.3 and ~494.7 eV, respectively, confirming the presence of the Sn^{4+} oxidation state[46,47]. In addition, the good symmetry of the peaks, showing no sub-components, suggests the absence of Sn^{2+}. The O 1s core level (Fig. 4b), in contrast, indicates the presence of two components, with the main peak at ~531 eV, assigned to the lattice oxygen, and a shoulder at ~532.5 eV, which is assigned to contamination (organic fragments) on the samples in light of the lack of additional structures on the Sn 3d core level[46]. Both WDX and XPS analysis showed no evidence of chlorine contamination and similar tin contents (anal. calcd. for SnO$_2$: Sn 33.27 and O 66.53 at.%, found WDX: Sn 30.18 at.%, found XPS: Sn 30.30 at.% with a O/Sn ratio of 1.9 taking into account only the component assigned to lattice oxygen). The formation of SnO$_2$ at this temperature is consistent with the TGA of SnCl$_4$·5H$_2$O, which has been shown to produce nearly stoichiometric tin oxide from 450 °C to 700 °C[41,48].

Au@SnO$_2$ NRs. The films synthesised at 620 °C by co-deposition *via* AACVD of tin and gold precursors dissolved in acetone resulted in the formation of adherent uniform greyish films on silicon substrates, with similar appearance to those deposited from only the tin precursor. SEM imaging of the Au@SnO$_2$ films revealed a high density of NRs (Fig. 5a) with similar features to those observed for intrinsic SnO$_2$ films deposited at 620 °C (Fig. 2), though with apparently small particles dispersed at the surface. Similarly, TEM imaging of the functionalised NRs displayed NPs along the NR surface (Fig. 5b,c), which indicate the incorporation of Au NPs as noticed previously when co-depositing gold with tungsten oxide nanoneedles[29]. The NPs showed spherical morphologies and sizes up to 35 nm; an analysis of the size distribution of these particles *via* TEM was complex due to NRs tending to agglomerate on the TEM grids and the relatively high thickness of NRs.

XRD of the Au@SnO$_2$ NRs (Fig. 6a) revealed similar pattern than that observed for intrinsic SnO$_2$ NRs (Fig. 1) showing a tetragonal phase (P42mnm space group, $a = 4.7382$ Å, $c = 3.1871$ Å; ICCD card no. 411-1445), with an extra weak diffraction at 44.3 degrees corresponding to the (200) reflections of gold face centred cubic phase (Fm3m space group, $a = 4.07860$ Å; ICCD card no. 04-0784). XPS of the films indicated a (0.9 at.%) 3.7 wt.% Au in the films with the characteristics of Au 4f core level spectra being in agreement with that reported for gold metal[29], which suggests the gold NPs incorporated at the surface of the tin oxide NRs are in the metallic state. The Au:Sn ratio determined by XPS (found: Au:Sn 3.22 at.% (5.23 wt.%)) and compared to the initial ratio present in the precursor solution used for AACVD (anal. calcd for Au:Sn 23.2 wt.%) showed the incorporation of gold NPs is about 23% efficient, which is higher compared to the efficiency (5%) obtained previously for the co-deposition of tungsten oxide and gold[30], likely due to the higher temperature of deposition.

SnO$_2$ and Au@SnO$_2$ NRs integrated into micromachined platforms. The SnO$_2$ and Au@SnO$_2$ films grown directly into the micromachined platforms (Fig. 7a) *via* AACVD at 620 °C, showed similar diffraction patterns (Fig. 7b) with NR-like morphology (Fig. 7c,d) compared to that observed for the same deposition conditions on silicon wafers (**section SnO$_2$ NRs and Au@SnO$_2$ NRs**). Measurements of the electrical resistance of the
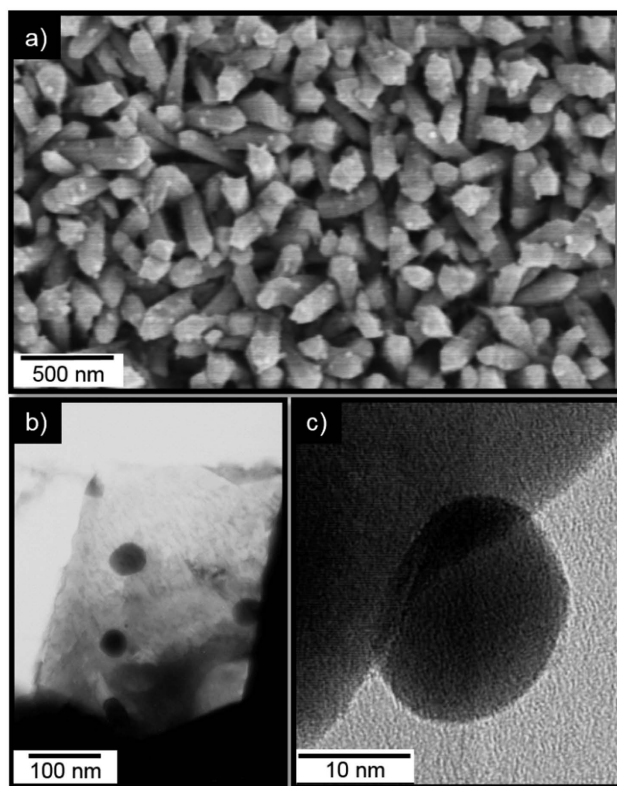
Figure 5. SEM (**a**) and TEM images at low (**b**) and high (**c**) magnification for the Au@SnO$_2$ NRs.
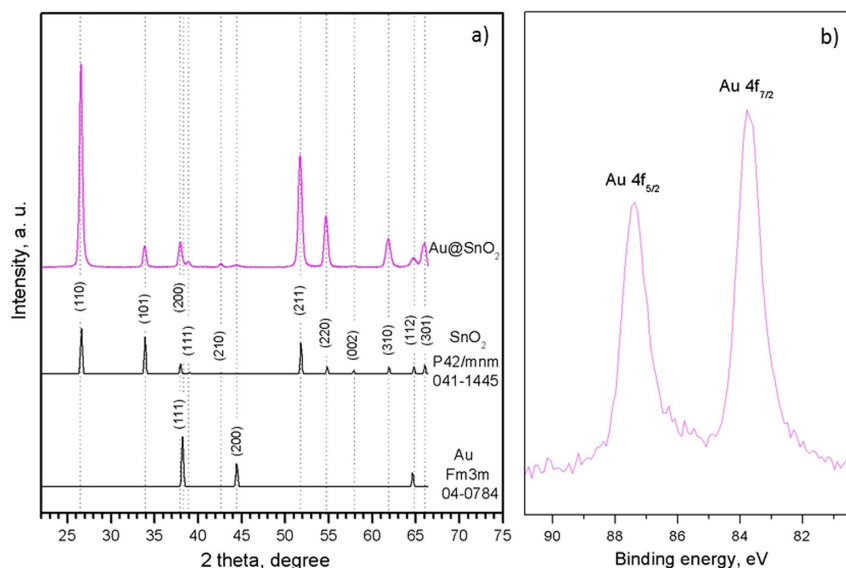

Figure 6. Typical XRD pattern of the Au@SnO$_2$ NRs (**a**) indexed to a tetragonal phase (P42/mnm, ICCD card no. 041-1445) of tin oxide and to the gold face centred cubic phase (Fm3m, ICCD card no. 04-0784). Au 4f core-level spectrum recorded on Au-functionalised tin oxide NRs (**b**).

films using the microelectrodes confirmed a good electrical contact, with the resistance at different sensor operating temperatures showing a direct dependency of the conductivity to the temperature, as expected for an n-type semiconductor. The apparent energy activation for electrical conduction (E_a^c) estimated for temperatures between 250 °C and 350 °C yielded a value of 0.35 eV for the SnO$_2$ NRs, which is consistent with the E_a^c for porous SnO$_2$ (between 0.28 eV and 1.1 eV) reported previously[49]. The E_a^c estimated for the Au@SnO$_2$ NRs, in contrast, yielded a
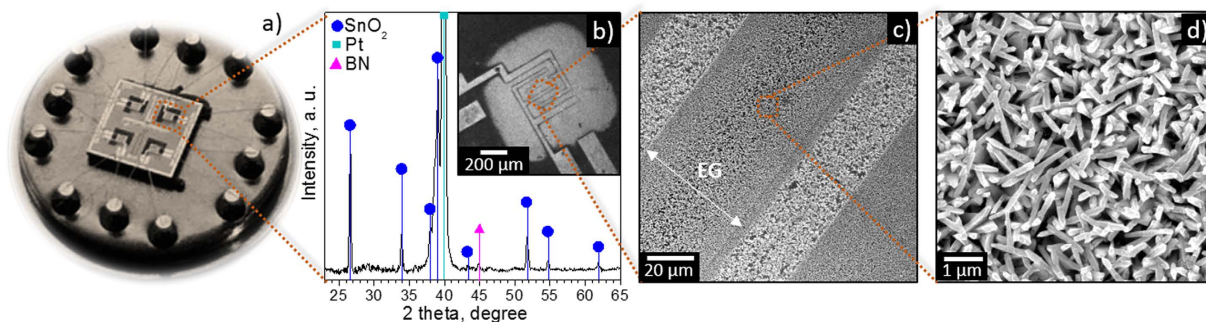
Figure 7. Photograph of the 4-microsensor array mounted on a standard TO-8 package (**a**), XRD of a single microsensor based on SnO_2 nanorods (platinum and boron nitride diffractions come from the microsensor platform) (**b**) and SEM images at low (**c**) and high (**d**) magnification of the SnO_2 material grown onto the microplatform (EG represents the electrode gap).

much lower value (0.11 eV), approximately 69% less than the obtained with the SnO_2 NRs. This change is much higher compared to that recorded previously for the co-deposited Au-functionalised tungsten oxide (Au@WO$_3$) structures, which showed only 9% lower E_a^c compared to the non-functionalised tungsten oxide structures[30]. These numbers show a close relation with the theoretical differences in the work functions (W_F) of these materials, as the W_F of Au (4.8 eV)[50] is 16% and 2% lower than that of SnO_2 (5.7 eV)[2] and WO_3 (4.9 eV)[51], respectively, and the relative value of these differences (i.e. 8) is similar to that found for the E_a^c of Au@SnO$_2$ and Au@WO$_3$ (i.e. 7.7).

Gas sensing characterization. Gas sensing tests were carried out to H_2 and CO at various operating temperatures between 250 and 390 °C using dc resistance measurements. The temperature dependency of the sensor response for each analyte and concentration is displayed in Fig. 8a and S3a. Results for H_2 suggest a similar trend for sensors composed of SnO_2 and Au@SnO$_2$ NRs, with slight changes of the response by increasing the operating temperature, whereas results for CO display a tendency to increase the sensor response by increasing the operating temperature, particularly for sensors comprised of Au@SnO$_2$ NRs. Figure 8a and S3a also reveal greater sensor responses for the Au-functionalised NRs compared to the intrinsic NRs, with higher increments (12-fold) for H_2 than for CO (2-fold), which reduces the cross-response of these analytes and in turn improves the selectivity of the device. The typical change of resistance recorded for each type of sensor is shown in Fig. 8b and S3b. Overall, the sensor responses displayed an n-type behaviour, i.e. decreasing electrical resistance when exposed to H_2 or CO. During the testing period (i.e. 100 h) the sensor response showed good reproducibility with standard errors below $\pm$1.5%, and little variation of the baseline resistance at each operating temperature (below $\pm$6%), with the SnO_2 NRs showing lower baseline resistances compared to the Au@SnO$_2$ NRs (e.g. 4.5 kΩ for SnO_2 and 50 kΩ for Au/SnO$_2$ at 290 °C). With the injection of humidity (90% RH) in the system, at operating temperature of 290 °C, the baseline resistance of the sensors increased up to 5.5 kΩ for sensors based on SnO_2 NRs and 120 kΩ for those based on Au@SnO$_2$ NRs. Under these conditions the electrical resistance changes to H_2 remained stable and reproducible, but the sensor response was higher compared to the response obtained in dry air (Fig. 8), showing an increase of the sensor response to H_2 up to 18% for the SnO_2 NRs and 140% for the Au@SnO$_2$ NRs, indicating decreased humidity tolerance of the SnO_2 NRs after decoration with gold NPs.

A detailed view of the normalised response to H_2 at 290 °C for the sensors based on SnO_2 and Au@SnO$_2$ NRs show the characteristics of the response (t_R) and recovery (t_{rec}) time, and the time needed to reach stationary state when exposed to H_2 (Fig. S4). The overall view of the response and recovery times as function of the temperature for each type of sensor towards H_2 (Fig. 9) suggests a decrease in the response and recovery time of the sensor as the operating temperature increases. Results in Fig. 9 also show faster response times for the Au@SnO$_2$ NRs compared to intrinsic NRs, and an inverse relationship of the recovery time with respect to the response time, i.e. longer recovery times for Au@SnO$_2$ as opposed to SnO_2. Similar comparison between the non-functionalised and Au-functionalised tungsten oxide structures studied previously showed a similar tendency of the response/recovery time[30].

After 100 h of testing the sensor alternately to H_2 and CO in dry and humid environment and at different operating temperatures, the gas sensitive nanostructures where examined again using SEM and XRD. In comparison to the initial samples the morphology of the SnO_2 and Au@SnO$_2$ NRs was unchanged and the diffraction patterns were identical, indicating a good stability of the devices.

Discussion

The AACVD of $SnCl_4$·5H_2O allowed for the synthesis of nanostructured SnO_2 films by adjusting the deposition temperature, the precursor concentration and solvent used to produce the aerosol. The ideal conditions for growing SnO_2 NRs were found using a solution 8.5 mM of $SnCl_4$·5H_2O dissolved in acetone at 620 °C (Fig. 2), a much lower temperature compared to other CVD methods based on VS mechanism which require temperatures exceeding 850 °C[10,11,13,14,25]. The AACVD of SnO_2 NRs *via* VS mechanism at this relatively low temperature can be connected to two factors: a drop of the energy activation for the perpendicular growth of the film registered when using acetone (16.2 kJ/mol) instead of methanol as carrier solvent, and a decrease of the number of precursor molecules per volume induced by reducing the initial solution concentration about 30%. This is consistent with
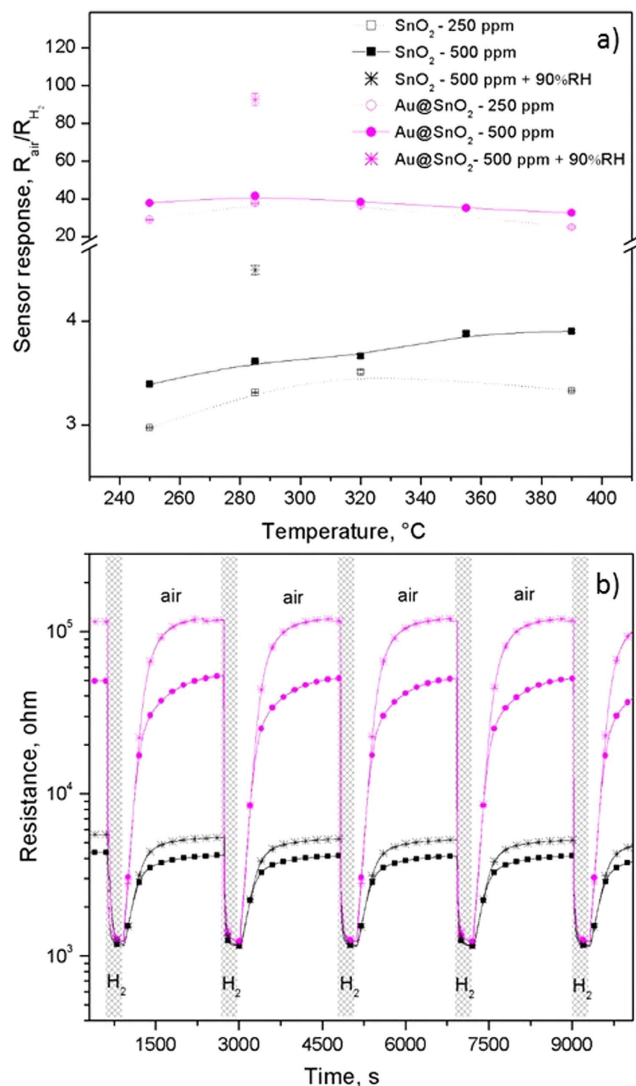
Figure 8. Sensor responses to 250 and 500 ppm of H_2 as a function of the operating temperature (**a**) and film-resistance changes towards 500 ppm of H_2 at 290 °C (**b**). The response to 500 ppm of H_2 in humidity (90% RH) is displayed in both plots.

previous analysis of the growth mechanism of tungsten oxide nanorods *via* AACVD, which indicated that the transition from planar to nanorod films (characterised by the Frank-van der Merwe and Volmer-Weber growth mode, respectively) at a fixed temperature requires the attenuation of these factors (i.e. E_a^d and density of precursor molecules)[43]. As the same deposition temperatures and AACVD parameters (e.g. flow, gas carrier, solution concentration) for the different systems were kept constant with the exception of the 'carrier' solvent, it is therefore reasonable to suggest that the use of solvents such as acetone and methanol, which can decompose *via* radical mechanism at these temperatures[52–54], might also add active reactive products to the reaction in AACVD. This has a direct influence on the decomposition profile of the tin precursor and in turn modifies the energy activation for the perpendicular growth rate of the film promoting formation of nanostructured growth. The presence of metallic tin at 600 °C when using a methanol solution (Fig. S1) corroborates this hypothesis, as this suggests a different chemical species, with a different decomposition profile to the initial precursor, is involved in the AACVD process when this solvent was used. Acetone may also play a similar role in the decomposition mechanism of the tin precursor but results suggest it is less reactive than methanol. The change in reactive chemical species is likely to affect the reaction time and hence the ratio between this and the reactor residence time, parameters which have previously been shown to be involved in the transition from planar to columnar-like structures[55].

The incorporation of a second precursor ($HAuCl_4 \cdot 3H_2O$) during the AACVD of SnO_2 NRs allowed for the co-deposition of Au@SnO_2 NRs, similar to our previous results for the co-deposition of gold NPs with tungsten oxide nanostructures[29,30], although requiring use of a different carrier solvent and higher deposition temperatures (acetone at 620 °C instead of methanol at 400 °C for tungsten oxide). Overall, the analysis of these structures showed that the gold NPs incorporated at the tin oxide NRs are in metallic state (Fig. 6b) with no evidence of modification of either the morphology (Fig. 5) or the crystalline structure (Fig. 6a) of the NRs. However, the
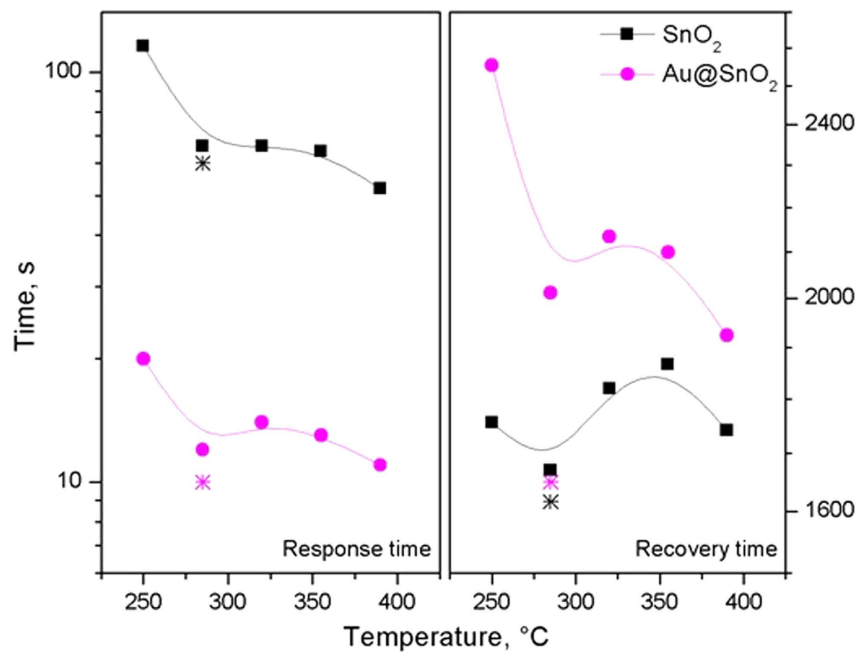
Figure 9. Response (**a**) and recovery (**b**) time for each type of sensor towards 500 ppm of H_2. The response and recovery times at 290 °C in humidity are also shown in the plot and represented by a star.

SnO$_2$	Method	Integration	Sensor platform	T_{op} °C	Gas	C ppm	R	t_{res} s	t_{rec} s	S %	Ref
NRs	**AACVD**	**direct**	**μM^P**	**290**	**H$_2$**	**250**	**3.3**	**70**	**1700**	**0.20**	**This work**
Grains	HT	transfer	Ceramic^P	400	H$_2$	2000	26	10	180	0.16	61
Grains	CVD	direct	Ceramic^P	300	H$_2$	100	1.03	–	–	–	63
NRs	TE	transfer	Si-based^P	200	H$_2$	250	1.9	–	–	0.17	64
NRs	**AACVD**	**direct**	**μM^P**	**290**	**CO**	**250**	**1.1**	**–**	**–**	**0.04**	**This work**
Grains	HT	transfer	Ceramic^T	300	CO	200	3	7.2	10.2	0.17	65
NWs	CVD	direct ^{seeds}	Ceramic^P	–	CO	400	3.9	10	–	–	66
fibers	ES	direct	Si-based^P	300	CO	10	6	–	–	0	67

Table 1. Summary of the gas sensing properties of non-functionalised tin oxide reported in the literature for H$_2$ and CO. NRs: nanorods, NWs: nanowires, HT: hydrothermal, TE: thermal evaporation, ES: electrospinning, seeds: gold catalytic seeds for the NW growth, μM: micromachined, P and T: planar and tubular architecture, T_{op}: sensor operating temperature, C: concetration, R: response (R_{air}/R_{gas}), t_{res}: response time, t_{rec}: recovery time, S: sensitivity estimated from each referenced work and defined as the ratio between the change in sensor response for a fixed change in analyte concentration.

lower energy activation of conduction (E_a^c) estimated for the Au@SnO$_2$ samples (0.11 eV) compared to that of the intrinsic SnO$_2$ (0.35 eV) may suggest the presence of Au-O bonds at the surface of the NPs, as inferred earlier for the co-deposited gold NPs on tungsten oxide[30].

The direct integration of these structures (SnO$_2$ and Au@SnO$_2$) with micromachined platforms was achieved, demonstrating this process and the associated temperature are compatible with the complementary electronics on these devices. The capability to integrate nanostructured materials with microsystems, such as those used in this work (i.e. fabricated by MEMS technology), represents a technological advantage for gas sensing, as MEMS sensor platforms provide low power consumption features and are suitable for integrating monolithic sensor arrays. Sensor testing showed an optimum operating temperature for SnO$_2$ of 300 °C, a temperature frequently reported for SnO$_2$ when sensing H$_2$ and CO, Table 1. At this temperature (i.e. 300 °C) the micromachined sensors registered 16-times less power consumption (32 mW) than the traditional planar ceramic sensors (525 mW) used in our previous works for tungsten oxide[29].

Overall, validation of these devices towards the detection of H$_2$ and CO showed good performance with stable signal, very low drift of electrical resistance over the testing period and relatively fast response. These characteristics are highly enhanced compared to our previous sensors based on SnO$_2$ NPs synthesised via AACVD of tin complexes[34]; which showed a very slow and low resistance change to NO$_2$ and non-sensitivity towards H$_2$ or CO. A direct comparison of our results and those of the literature is relatively complex, as the performance of the

sensor is not only linked to the material properties, but also in part to the characteristics of the transducers and test conditions (e.g., operating temperatures, flows, and gas concentrations). Despite this we believe that Table 1 can still be useful to evaluate the tendency of SnO_2 towards the analytes tested in this work. Consequently, this comparative table suggests that the SnO_2 NRs synthesised *via* AACVD provide higher sensitivity (S) to H_2 compared to that recorded in other works for this analyte. In contrast, the sensitivity obtained for CO reveals a much lower value with respect to that observed for hydrothermal synthesised grains, although marginally higher than that reported for electrospun tin oxide fibres. These differences could be linked to some technological characteristics of each sensor, for instance the use of platinum top electrodes in the sensor architecture of the electrospun films, or the use of transfer steps and most likely the introduction of impurities when integrating the tin oxide films synthesized *via* hydrothermal or thermal evaporation method into the sensor platforms. In fact, impurities such as chlorine (typically introduced from the precursors), or potassium and calcium (often introduced by the use of transfer steps) have been demonstrated to play a relevant role in the surface activity and sensing properties of tin oxide[56]; most of the tin oxide films in Table 1 were synthesised from chlorine containing precursors (i.e. $SnCl_4$ and $SnCl_2$) or integrated using transfer steps. The analysis of our SnO_2 NRs integrated directly on the micromachined platform though showed no evidence of chlorine, likely due to easy elimination *via* HCl from the $SnCl_4 \cdot 5H_2O$ precursor.

The shape and geometry of the AACVD NRs showed similar characteristics to those reported previously in prism-like rods[45], suggesting a surface likely dominated by the SnO_2 {110} facets. The presence of these facets, which have shown to be less favourable for CO adsorption due to the need of a particular adsorption geometry with the C-end orientated to the surface[2], may be responsible for the attenuation of the response to CO compared to H_2. No equivalent studies were found for H_2, however as the adsorption of H_2 includes the formation of intermediate molecules as water, and these have shown more favourable adsorption on SnO_2{110} surfaces[2], the higher responses registered for H_2 in dry and humid air seem consistent.

The functionalization of the SnO_2 NRs with Au NPs showed enhanced sensing characteristics, compared to the intrinsic SnO_2 NRs, which include higher sensor response, (almost 12- and 2-times more for H_2 and CO respectively) and a reduction of the response time of about 6 times. However, the functionalization also showed a tendency to reduce the sensor tolerance to humidity, inducing a larger change of the response to hydrogen in humid ambient compared to the non-functionalised SnO_2 NRs. This characteristic is undesirable in gas sensing and seems to be related to both the propensity of SnO_2 to adsorb hydroxyl groups on the surface at the temperature used for this test[57], and the amplification of the response by analogous mechanisms than those involved in the enhancement of H_2 and CO sensing. The mechanisms that lead the metal NPs functionalised SMOx to an enhanced gas sensing performance has been discussed in the literature previously, and generally involve surface dependent effects (i.e. chemical sensitization, which may include mechanisms such as spill-over and complementary decomposition) and/or interface dependent effects (electronic sensitization, which may include the modulation of potential barrier heights, carrier injection and conduction channel modulation)[58–60]. The faster response in the $Au@SnO_2$ compared to the SnO_2 NRs gives evidence of a chemical sensitization, with the Au NPs most likely accelerating the dissociation of hydrogen molecules into H atoms and simultaneously inducing a faster saturation of the active sites on the NR surface *via* spill-over. This saturation (also observed in the response (Fig. S4) of the sensors based on $Au@SnO_2$ NRs as opposed to those based on SnO_2 NRs) is responsible for the larger desorption time required to recover the baseline resistance at each temperature (Fig. 9). In contrast, the lower E_a^c obtained for the $Au@SnO_2$ NRs compared to the SnO_2 NRs indicates an electronic sensitization, with the Au NPs facilitating the carrier injection and thus modulating the conduction channel along the nanostructure.

The ratio of the response to H_2 and CO for each microsensor ($\Delta R = 2.5$ for SnO_2 and $\Delta R = 20$ for Au/SnO_2) indicates relatively higher cross-sensitivities for the microsensors comprised of intrinsic SnO_2 NRs, as opposed to those comprised of $Au@SnO_2$ NRs, which potentially improves selectivity to H_2. A comparison of these ratios with those recorded for similar systems synthesised *via* sol-gel in the literature[61] revealed similar values for the SnO_2 NRs and nearly 7 times higher values for the $Au@SnO_2$ NRs, suggesting the functionalisation of SnO_2 with Au NPs *via* AACVD is effective for improving the selectivity of tin oxide towards H_2 and CO.

In summary, these results demonstrate the AACVD of SnO_2 NRs *via* VS mechanism at exceptionally reduced process temperature compared to existing CVD methods with no need for substrate pre-treatment. This allowed for the direct integration of these nanostructures into micromachined platforms and their use for sensing H_2 and CO. The incorporation of Au NPs at the surface of the SnO_2 NRs *via* co-deposition improved the functionality of SnO_2, particularly to H_2, reducing the cross-sensitivity of this analyte to CO.

Conclusions

SnO_2 NRs with an aspect ratio of approximately 7 were synthesized without catalyst seeds *via* AACVD of $SnCl_4 \cdot 5H_2O$ at 620 °C, a much lower onset temperature compared to other CVD methods based on a VS mechanism, which typically requires temperatures exceeding 850 °C. The evolution of nanorod SnO_2 is linked to an increase in energy activation of the perpendicular growth of about 40% respect to that observed for non-nanostructured SnO_2 films, and is attributed to the use of acetone as solvent carrier, and a reduction of precursor concentration. Co-deposition of Au NPs (<35 nm) and SnO_2 NRs *via* AACVD was also achieved at 620 °C. The gas microsensors based on the intrinsic SnO_2 and $Au@SnO_2$ NRs were validated towards H_2 and CO and show sensing properties that are in agreement with the literature, with notable enhancement of sensing properties for $Au@SnO_2$ NRs which showed 12-fold higher response with 6-fold faster response and improved selectivity to H_2 compared to the gas sensors based on intrinsic SnO_2 NRs.

Experimental Section

SnO_2 synthesis. SnO_2 nanostructures were deposited at temperatures between 300 and 675 °C *via* aerosol assisted (AA) CVD of tin (IV) chloride pentahydrate ($SnCl_4 \cdot 5H_2O$, Sigma-Aldrich, ≥98%) dissolved in

15 ml of acetone. In order to vary the concentration of the solution, three different weights (45, 30 and 15 mg) of $SnCl_4\cdot5H_2O$ were used for the deposition. A piezoelectric ultrasonic atomiser (Liquifog, Johnson Matthey) operating at 1.6 MHz was used to generate an aerosol of the solution. The aerosol droplets were transported to the heated substrate by a nitrogen (BOC, oxygen free) gas flow (200 $cm^3\cdot min^{-1}$), and the time taken to transport the entire volume of solution was typically 15 minutes.

Au@SnO_2 synthesis.   Nanocomposites composed of gold NPs and tin oxide NRs were synthesised at 620 °C by co-deposition, *via* AACVD, of tin (IV) chloride pentahydrate (30 mg, $SnCl_4.5H_2O$, Sigma-Aldrich, ≥98%) and tetrachloroauric acid trihydrate (4.2 mg, $HAuCl_4\cdot3H_2O$, Sigma-Aldrich, 99.9%) dissolved in acetone (15 ml, Sigma-Aldrich, ≥99.6%) using the same system described above and following the method reported in literature[29].

Substrate and micromachined platforms.   Silicon wafers (10 mm × 10 mm × 0.37 mm) and KBr disks were used as substrates for film analysis, whereas micromachined platforms consisting of an array of four SiO_2/Si_3N_4/SiO_2 membrane, each of them with isolated polysilicon heaters and platinum electrodes (gap: 50 μm, thick: 0.2 μm), were used for gas sensor fabrication. After deposition of the sensing active film the platforms were mounted on a TO8 package. The sensor technology was described in detail previously[62].

Film analysis.   The morphology of the samples was examined using Scanning Electron Microscopy (SEM — Jeol 6301F, 5 keV). The structure using X-Ray Diffraction (either XRD — Bruker, AXD D8- Discover for the films grown on silicon wafers or Rigaku Smartlab 9 kW for the films grown on micromachined platfoms) and the chemical composition using Wavelength Dispersive X-Ray (WDX — Philips, XL30ESEM) and X-ray Photoelectron spectroscopy (XPS) (Thermo Scientific K-Alpha, using Al Ka radiation operated at 0.6 eV with electron gun operating at 1 eV and argon-ion gun operated at 10 eV; the binding energies were calibrated to the C 1s peak at 284.5 eV). TEM (JEOL JEM-100CX II, 100 kV) images were carried out on samples prepared by deposition on KBr substrates followed by dissolution of the substrate in distilled water and suspended on Cu grids.

Gas sensing tests.   Gas sensors were tested in a continuous flow (200 sccm) test chamber (280 cm^3) as previously described[62]. The sensors were exposed to 250 and 500 ppm of hydrogen and carbon monoxide for 10 min and subsequently the chamber purged with air until initial baseline resistance was recovered. The whole testing period comprised of 100 h during which sensors were tested to different hydrogen and carbon monoxide concentrations at operating temperatures between 250 and 390 °C in dry and humid ambient, performing 5 replicates for each condition. To obtain the desired analyte concentration calibrated cylinders of either hydrogen (Praxair, 1000 ppm) or carbon monoxide (Praxair, 1000 ppm) were mixed with pure synthetic air (Carburos Metálicos, 99.99%) by means of a mass flow system (Bronkhorst hi-tech 7.03.241). The sensor response was defined as $R = R_a/R_g$, where R_a is the sensor resistance in air at stationary state and R_g represents the sensor resistance after 10 min of the analyte exposure. The response time was defined as the time required for the sensor to reach 90% of the sensor response, and the recovery time as the time required to reach 10% of the initial baseline resistance after the analyte was purged.

References
1. Bhushan, B. *Springer Handbook of Nanotechnology* (Springer, Verlag, 2004).
2. Batzill, M. & Diebold, U. The surface and materials science of tin oxide. *Prog. Surf. Sci.* **79,** 47–154 (2005).
3. Pan, J., Shen, H. & Mathur, S. One-Dimensional SnO_2 Nanostructures: Synthesis and Applications. *J. Nanothecnology* **2012,** 12 (2012).
4. Barth, S., Hernandez-Ramirez, F., Holmes, J. D. & Romano-Rodriguez, A. Synthesis and applications of one-dimensional semiconductors. *Prog. Mater Sci.* **55,** 563–627 (2010).
5. McAleer, J. F., Moseley, P. T., Norris, J. O. W., Williams, D. E. & Tofield, B. C. Tin Dioxide Gas Sensors. Part 2.-The Role of Surface Additives. *J. Chem. Soc., Faraday Trans.* 1, **84,** 441–457 (1988).
6. Vallejos, S., Di Maggio, F., Shujah, T. & Blackman, C. Chemical vapour deposition of gas sensitive metal oxides. *Chemosensors* **4,** 4 (2016).
7. Ma, Y.-J., Zhou, F., Lu, L. & Zhang, Z. Low-temperature transport properties of individual SnO_2 nanowires. *Solid State Commun.* **130,** 313–316 (2004).
8. Mathur, S., Barth, S., Shen, H., Pyun, J.-C. & Werner, U. Size-Dependent Photoconductance in SnO_2 Nanowires. *Small* **1,** 713–717 (2005).
9. Pan, J., Xiao, L., Shen, H. & Mathur, S. In *Nanostructured Materials and Nanotechnology III* 9–15 (John Wiley & Sons, Inc., 2010).
10. Thabethe, B. S., Malgas, G. F., Motaung, D. E., Malwela, T. & Arendse, C. J. Self-Catalytic Growth of Tin Oxide Nanowires by Chemical Vapor Deposition Process. *J. Nanomaterials* **2013,** 7 (2013).
11. Qu, D. M. *et al.* Nanowires and nanowire–nanosheet junctions of SnO_2 nanostructures. *Mater. Lett.* **61,** 2255–2258 (2007).
12. Qin, D., Yan, P., Li, G., Xing, J. & An, Y. Self-construction of SnO_2 cubes based on aggration of nanorods. *Mater. Lett.* **62,** 2411–2414 (2008).
13. Ahn, J.-H., Wang, G. & Kim, Y.-J. Facile synthesis of tin oxide nanofibres. *Current Applied Physics* **9,** e176–e179 (2009).
14. Butt, F. K. *et al.* Metal-catalyzed synthesis of ultralong tin dioxide nanobelts: Electrical and optical properties with oxygen vacancy-related orange emission. *Mater. Sci. Semicond. Process.* **26,** 388–394 (2014).
15. Müller, R. *et al.* Influence of precursor chemistry on morphology and composition of CVD-grown SnO_2 nanowires. *Chem. Mater.* **24,** 4028–4035 (2012).
16. Dai, Z. R., Pan, Z. W. & Wang, Z. L. Novel nanostructures of functional oxides synthesized by thermal evaporation. *Adv. Funct. Mater.* **13,** 9–24 (2003).
17. Budak, S., Miao, G. X., Ozdemir, M., Chetry, K. B. & Gupta, A. Growth and characterization of single crystalline tin oxide (SnO_2) nanowires. *J. Cryst. Growth* **291,** 405–411 (2006).
18. Dai, Z. R., Gole, J. L., Stout, J. D. & Wang, Z. L. Tin oxide nanowires, nanoribbons, and nanotubes. *J. Phys. Chem. B* **106,** 1274–1279 (2002).
19. Wang, B., Yang, Y. H., Wang, C. X. & Yang, G. W. Nanostructures and self-catalyzed growth of SnO_2. *J. Appl. Phys.* **98** (2005).
20. Liu, Z. *et al.* Laser ablation synthesis and electron transport studies of tin oxide nanowires. *Adv. Mater.* **15,** 1754–1757 (2003).

21. Kolmakov, A., Zhang, Y., Cheng, G. & Moskovits, M. Detection of CO and O_2 using tin oxide nanowire sensors. *Adv. Mater.* **15,** 997–1000 (2003).
22. Zheng, M. *et al.* Fabrication and structural characterization of large-scale uniform SnO_2 nanowire array embedded in anodic alumina membrane. *Chem. Mater.* **13,** 3859–3861 (2001).
23. Jiang, X., Wang, Y., Herricks, T. & Xia, Y. Ethylene glycol-mediated synthesis of metal oxide nanowires. *J. Mater. Chem.* **14,** 695–703 (2004).
24. Vayssieres, L. & Graetzel, M. Highly ordered SnO_2 nanorod arrays from controlled aqueous growth. *Angew. Chem. Int. Ed.* **43,** 3666–3670 (2004).
25. Liu, Y. & Liu, M. Growth of aligned square-shaped SnO_2 tube arrays. *Adv. Funct. Mater.* **15,** 57–62 (2005).
26. Yamazoe, N., Sakai, G. & Shimanoe, K. Oxide semiconductor gas sensors. *Catal. Surv. Asia* **7,** 63–75 (2003).
27. Vallejos, S., Gràcia, I., Figueras, E. & Cané, C. Catalyst-free vapor-phase method for direct Integration of gas sensing nanostructures with polymeric transducing platforms. *J Nanomaterials* **2014,** 9 (2014).
28. Hou, X. & Choy, K. L. Processing and Applications of Aerosol-Assisted Chemical Vapor Deposition. *Chem. Vap. Deposition* **12,** 583–596 (2006).
29. Vallejos, S. *et al.* Au nanoparticle-functionalised WO_3 nanoneedles and their application in high sensitivity gas sensor devices. *Chem. Commun.* **47,** 565–567 (2011).
30. Vallejos, S. *et al.* Single-step deposition of Au- and Pt-nanoparticle-functionalized tungsten oxide nanoneedles synthesized via aerosol-assisted CVD, and used for fabrication of selective gas microsensor arrays. *Adv. Funct. Mater.* **23,** 1313–1322 (2013).
31. Annanouch, F. E. *et al.* Aerosol-assisted CVD-grown WO_3 nanoneedles decorated with copper oxide nanoparticles for the selective and humidity-resilient detection of H_2S. *ACS Appl. Mater. Inter.* **7,** 6842–6851 (2015).
32. Vallejos, S., Gràcia, I., Figueras, E. & Cané, C. Nanoscale heterostructures based on $Fe_2O_3@WO_{3-x}$ nanoneedles and their direct integration into flexible transducing platforms for toluene sensing. *ACS Appl. Mater. Inter.* **7,** 18638–18649 (2015).
33. Zhao, J. *et al.* Tin oxide thin films prepared by aerosol-assisted chemical vapor deposition and the characteristics on gas detection. *Sens. Actuators, B* **145,** 788–793 (2010).
34. Stoycheva, T. T. *et al.* Aerosol-assisted CVD of SnO_2 thin films for gas-sensor applications. *Chem. Vap. Deposition* **17,** 247–252 (2011).
35. Wildsmith, T., Hill, M. S., Johnson, A. L., Kingsley, A. J. & Molloy, K. C. Exclusive formation of SnO by low temperature single-source AACVD. *Chem. Commun.* **49,** 8773–8775 (2013).
36. Syed Mansoor, A., Syed Tajammul, H., Shahzad Abu, B., Jan, M. & Naeem ur, R. Effect of doping on the structural and optical properties of SnO_2 thin films fabricated by aerosol assisted chemical vapor deposition. *J. Phys.: Conf. Ser.* **439,** 012013 (2013).
37. Khan, N. *et al.* Synthesis and characterization of iron tin oxide thin films from single source bimetallic precursors. *Polyhedron* **69,** 40–47 (2014).
38. Chew, C., Bishop, P., Salcianu, C., Carmalt, C. J. & Parkin, I. P. Aerosol-assisted deposition of gold nanoparticle-tin dioxide composite films. *RSC Adv.* **4,** 13182–13190 (2014).
39. Dharmadasa, R., Wijayantha, K. G. U. & Tahir, A. A. ZnO–SnO_2 composite anodes in extremely thin absorber layer (ETA) solar cells. *J. Electroanal. Chem.* **646,** 124–132 (2010).
40. Bhachu, D. S., Waugh, M. R., Zeissler, K., Branford, W. R. & Parkin, I. P. Textured fluorine-doped tin dioxide films formed by chemical vapour deposition. *Chemistry – A European Journal* **17,** 11613–11621 (2011).
41. van Mol, A. M. B., Chae, Y., McDaniel, A. H. & Allendorf, M. D. Chemical vapor deposition of tin oxide: Fundamentals and applications. *Thin Solid Films* **502,** 72–78 (2006).
42. Tucic, A., Marinkovic, Z. V., Mancic, L., Cilense, M. & Milošević, O. Pyrosol preparation and structural characterization of SnO_2 thin films. *J. Mater. Process. Technol.* **143–144,** 41–45 (2003).
43. Ling, M. & Blackman, C. Growth mechanism of planar or nanorod structured tungsten oxide thin films deposited via aerosol assisted chemical vapour deposition (AACVD). *Phys. Status Solidi C* **12,** 869–877 (2015).
44. Dawei, Y. & Baojun, L. The study of rf plasma activated processes for stannic oxide thin film deposition. *Vacuum* **42,** 919–922 (1991).
45. Han, X. *et al.* Synthesis of tin dioxide octahedral nanoparticles with exposed high-energy {221} facets and enhanced gas-sensing properties. *Angew. Chem.* **121,** 9344–9347 (2009).
46. Das, S., Kim, D.-Y., Choi, C.-M. & Hahn, Y. B. Structural evolution of SnO_2 nanostructure from core–shell faceted pyramids to nanorods and its gas-sensing properties. *J. Cryst. Growth* **314,** 171–179 (2011).
47. Liu, X., Zhang, J., Guo, X., Wang, S. & Wu, S. Core-shell [small alpha]-$Fe_2O_3@SnO_2$/Au hybrid structures and their enhanced gas sensing properties. *RSC Adv.* **2,** 1650–1655 (2012).
48. Patil, P. S., Kawar, R. K., Seth, T., Amalnerkar, D. P. & Chigare, P. S. Effect of substrate temperature on structural, electrical and optical properties of sprayed tin oxide (SnO_2) thin films. *Ceram. Int.* **29,** 725–734 (2003).
49. McAleer, J. F. *et al.* Tin oxide based gas sensors. *Mater. Chem. Phys.* **17,** 577–583 (1987).
50. Sergio, T. Work function, electronegativity, and electrochemical behaviour of metals: II. Potentials of zero charge and "electrochemical" work functions. *J. Electroanal. Chem. Interfacial Electrochem.* **33,** 351–378 (1971).
51. He, T. & Yao, J. Photochromic materials based on tungsten oxide. *J. Mater. Chem.* **17,** 4547–4557 (2007).
52. McNesby, J. R., Davis, T. W. & Gordon, A. S. Pyrolisis of mixtures of acetone and acetone-d6. *J. Am. Chem. Soc.* **76,** 823–827 (1954).
53. Jasper, A. W., Klippenstein, S. J., Harding, L. B. & Ruscic, B. Kinetics of the reaction of methyl radical with hydroxyl radical methanol decomposition. *J. Phys. Chem. A.* **111,** 3932–3950 (2007).
54. Norton, T. S. & Dryer, F. L. Towards a comprehensive mechanism for methanol pyrolisis. *Int. J. Chem. Kinet.* **22,** 219–241 (1990).
55. An, W. J., Thimsen, E. & Biswas, P. Aerosol-chemical vapor deposition method for synthesis of nanostructured metal oxide thin films with controlled morphology. *J. Phys. Chem. Lett.* **1,** 249–253 (2009).
56. Pavelko, R. G., Yuasa, M., Kida, T., Shimanoe, K. & Yamazoe, N. Impurity level in SnO_2 materials and its impact on gas sensing properties. *Sens. Actuators, B* **210,** 719–725 (2015).
57. Korotcenkov, G., Blinov, I., Brinzari, V. & Stetter, J. R. Effect of air humidity on gas response of SnO_2 thin film ozone sensors. *Sens. Actuators, B* **122,** 519–526 (2007).
58. Roldan Cuenya, B. Synthesis and catalytic properties of metal nanoparticles: Size, shape, support, composition, and oxidation state effects. *Thin Solid Films* **518,** 3127–3150 (2010).
59. Hübner, M. *et al.* The structure and behavior of platinum in SnO_2-based sensors under working conditions. *Angew. Chem. Int. Ed.* **50,** 2841–2844 (2011).
60. Miller, D. R., Akbar, S. A. & Morris, P. A. Nanoscale metal oxide-based heterojunctions for gas sensing: a review. *Sens. Actuator, B* **204,** 250–272 (2014).
61. Yin, X.-T. & Guo, X.-M. Sensitivity and selectivity of (Au, Pt, Pd)-loaded and (In, Fe)-doped SnO_2 sensors for H_2 and CO detection. *J Mater Sci: Mater Electron* **25,** 4960–4966 (2014).
62. Vallejos, S. *et al.* Micro-machined WO_3-based sensors selective to oxidizing gases. *Sens. Actuator B* **132,** 209–215 (2008).
63. Ansari, S. G., Gosavi, S. W., Gangal, S. A., Karekar, R. N. & Aiyer, R. C. Characterization of SnO_2-based H_2 gas sensors fabricated by different deposition techniques. *J Mater Sci: Mater Electron* **8,** 23–27 (1997).
64. Shen, Y. *et al.* Synthesis of SnO_2 nanorods and application to H_2 sensor. *J. Alloys Compd.* **593,** 271–274 (2014).

65. Li, C., Lv, M., Zuo, J. & Huang, X. SnO$_2$ highly sensitive CO gas sensor based on quasi-molecular-imprinting mechanism design. *Sensors* **15,** 3789 (2015).
66. Trung, D. D. *et al.* Effective decoration of Pd nanoparticles on the surface of SnO$_2$ nanowires for enhancement of CO gas-sensing performance. *J. Hazard. Mater.* **265,** 124–132 (2014).
67. Katoch, A., Byun, J.-H., Choi, S.-W. & Kim, S. S. One-pot synthesis of Au-loaded SnO$_2$ nanofibers and their gas sensing properties. *Sens. Actuators, B* **202,** 38–45 (2014).

Acknowledgements

Author Contributions

S.V. and C.B. wrote the main manuscript text. S.V., S.S., F.E.A., I.G., E.L. and C.B. were involved in the experimental work and/or results analysis, and reviewed the manuscript.

Additional Information

Supplementary information accompanies this paper at http://www.nature.com/srep

Competing financial interests: The authors declare no competing financial interests.

How to cite this article: Vallejos, S. *et al.* Aerosol assisted chemical vapour deposition of gas sensitive SnO$_2$ and Au-functionalised SnO$_2$ nanorods via a non-catalysed vapour solid (VS) mechanism. *Sci. Rep.* **6**, 28464; doi: 10.1038/srep28464 (2016).